Rotordynamic Validation of a Twin Rotor-bearing System Considering Gyroscopic Forces and Bearing Dynamics with a Multibody Formulation: Application to a Geared UHBR Gas Turbine

T. S. Müller and H. Hennings, Institute of Aeroelasticity, German Aerospace Center, Bunsentraße 10, 37073, Göttingen, Germany

Abstract—A rotordynamic study for an engine with an ultra-high bypass ratio (BPR=17) was performed using a multibody (Simpack) and a finite element (Ansys) description. The previous validation based on an analytical system of a coaxial counter rotating twin rotor model was performed to legitimize the use of Simpack and the methodological approach, which included the modal reduction of finite element bodies and their integration in the multibody description. Therefore the eigenfrequencies as a function of the rotational speed and the unbalance respond due to eccentricity were compared. The same methodology was then applied to the UHBR engine. Performing an evaluation of the critical speed map, Campbell diagram and an unbalance respond analysis to identify the system behavior. By examining the system respond due to an unbalance force the need of a full modal description of the rotating parts with respect to a suspension point of the complete engine was shown.

NOMENCLATURE

{}	=	Matrix
x,y	=	Translational Coordinates
φ	=	Angle
M	=	Mass Matrix
C	=	Damping Matrix
K	=	Stiffness Matrix
G	=	Gyroscopic Matrix
F	=	Force
ρ	=	Density
n	=	Rotational Speed Ratio
k	=	Stiffness Parameter
d	=	Damping Parameter
ω	=	Eigenfrequency
Ω	=	Rotational Veclocity
$m_u d$	=	Mass Unbalance
LP	=	Low Pressure
HP	=	High Pressure

Subscripts

d	=	Disk
r	=	Rotorshaft
n	=	nth-Element
b	=	Bearing
s	=	System
x,y	=	Axis of Rotation
$\dot{}$	=	Velocity
$\ddot{}$	=	Acceleration

1 INTRODUCTION

To meet the growing demands for air travel in major economic areas and thus increase the capacity limits, it is essential to establish efficient point-to-point connections thereby reducing the travel time. At the same time, meeting economical aspects and demands, such as fuel consumption, there is a more efficient technology required. Whereby socio-ecological aspects, primarily the reduction of the emission CO_2 and noise have to be addressed. The Collaborative Research Center 880 devoted itself to the investigation of those fundamental issues. Thematically, the areas are divided into specific research projects, each focusing on different aspects of a common future aircraft configuration (figure 1, Radespiel and Heinze (2013)). Broadly divided, the research program is organized thematically in four topics: "Aeroacoustic Basics", "Efficient High-lift", "Flight Dynamics" and "Aircraft Design and Technology Assessment".

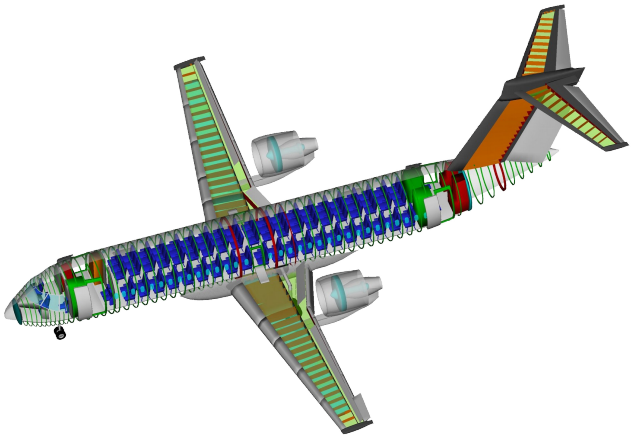

Fig. 1. Principal setup of the current configuration (Radespiel and Heinze, 2013)

For the sake of an increased efficiency, less direct operating cost and higher flight safety the investigated engine from the first funding period was changed from a twin-spool turbo engine with open rotor concept to a gas turbine with an ultra-high bypass ratio (BPR = 17) mounted on the upper surface of the wing for the current, second funding period. In this context the focus lies on a fundamental phenomenon, the flutter of wings structures, which is a dynamic instability due to the coupling of structural and aerodynamic forces. Once induced, flutter motion of a structure can lead to complete destruction.

Therefore there is a need for a precise tool for an accurate stability analysis conducting the preliminary aircraft design and thus providing the opportunity to be able to intervene consciously in the process of development. On that account there is a reduced order model (ROM) for flutter predictions with a nodal approach developed, (Krukow and Dinkler, 2014). Due to the large rotating masses it is assumed that the mere description of the engine as a mass point is insufficient in order to capture its influence on the wing structure. Therefore a model of the overall dynamics of the engine has to be enclosed in the ROM, including gyroscopic and centrifugal forces and also forces induced by the thrust vector causing the structure to stiffen and change its modal characteristics, (Waitz and Hennings, 2015). Hence the modeling of the UHBR engine is approached in a hybrid way. For that reason a multibody formulation with the tool Simpack, and the modal reduced FE bodies, created with the FEM tool Ansys, after the Craig-Bampton method (Craig and Bampton, 1986) by the use of the substructure technique, were utilized.

The hybrid use of multibody systems in combination with finite element structures provides the potential to describe the global behavior in moving reference systems with regarding large deformations and the coupling of multiple kinematic chains of the entire engine and the connection to the wing. Furthermore the FEM interface enables the capturing of the elastic behavior of the rotor structures and the change in their own behavior by stiffening effects due to centrifugal and gyroscopic effects by importing their modal description. Since the calculation of the flexible body takes place under distinctive centrifugal forces, it is necessary to verify the general description of this particular multibody system with established programs to a simple system with analytical solutions. Besides the necessity for accuracy the numerical effort needs to be kept to a minimum of complexity. Therefore the amount of degrees of freedom for the built up of the UHBR model needs to be optimized.
In order to meet these requirements and legitimize the procedure a model for validation is needed. For this purpose, an adequate system was presented by Ferraris et al. (1996), a coupled dual rotor system, to work as a reference system with analytical results. Due to the simplicity of the model it served as an optimization system, in a modified form, for startup behavior (Fei et al., 2013). Additionally (Chiang and Hsu, 2004) investigated the influence of the rotational speed ratio on the critical speed. Accordingly it is a reliable and well-studied system which serves as a good validation model. Consequently, the prior aim of this paper is to model this simple unbalanced coaxially mounted counter-rotating twin-rotor system in Simpack and Ansys. The rotor dynamic analysis provides the natural frequencies taken as a function of rotational speed in form of Campbell diagrams and the response behavior due to an unbalance excitation considering tumbling behavior is investigated. The validation criterion lies in the accuracy of the modal description. It legitimatizes the use of Simpack and serves as a preparation for the methodology. Since there have not been any investigations of UHBR engines with multibody formulation the second aim of this paper is the modeling of a geared twin-shaft UHBR engine considering non-linear bearing dynamics in Simpack using the sub modeling technique. Finally a full rotordynamic analysis of the system is carried out, including a critical speed map, Campbell diagram, unbalance force and the behavior of the complete system on a startup.

2 Dynamics of Rotating Structures

To study rotor dynamic effects a typical system consists of an arbitrary number of rotor disks connected to a shaft which rotates with an angular velocity Ω and is mounted on discrete bearing which withstand the forces, (Gasch et al., 2005).

2.1 Single Rotor - Governing Equations

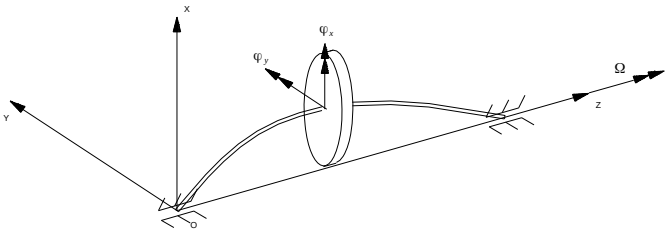

Fig. 2. Single rotor model (Laval rotor)

Figure 2 shows an elementary rotor-bearing system, a so called Laval rotor. It only consists of a single rotating shaft with a single mounted disk. The model is considered as a 2D problem preliminarily only taking the lateral displacements into account. The shaft is considered flexible and the disk is assumed to be a rigid body. Hereafter the equations of motion are explained.

2.1.1 Rigid Disk

The nodal coordinates for the center of the disk, represented by the following equation:

$$\{u^d\} = \{x^d, y^d, \varphi_x^d, \varphi_y^d\} \tag{1}$$

neglecting the displacement in the direction of the rotational axis. Under the assumption of a rigid connection to the rigid disk, the equation of motion can be described as:

$$[M^d]\{\ddot{u}^d\} + [G^d]\{\dot{u}^d\} = \{F^d\} \tag{2}$$

The total force imposed on the shaft consists of the inertia and the gyroscopic forces.

2.1.2 Flexible Shaft

Assuming the rotor consists of n finite elements:

$$\{u^r\} = \{x_n^r, y_n^r, \varphi_x^r, \varphi_y^r\} \tag{3}$$

The equation for the rotor is given by,

$$\begin{aligned}[M^r]\{\ddot{u}^r\} + ([G^r] + [C^r])\{\dot{u}^r\} \\ +([K^r] - [K_c^r])\{u\} = \{F^r\}\end{aligned} \tag{4}$$

whereas inertia, gyroscopic, damping and stiffening forces are taken into account.

2.1.3 Bearing Forces

Considering the bearing behavior to be non-depended of the rotational velocity Ω the bearing forces obey the governing equation of the following form:

$$[C^b]\{\dot{u}^b\} + [K^b]\{u^b\} = \{F^b\} \tag{5}$$

For the application in the second part of this work the bearing coefficients vary with the rotational velocity Ω.

2.2 System Equation of Motion

2.2.1 Single Rotor System

Bringing together component wise the formulation of eq. 2 - eq. 4, this leads to the following formulation:

$$[M^s]\{\ddot{u}^s\} + ([G^s] + [C^s])\{\dot{u}^s\} + ([K^s] - [K_c^s])\{u\} = \{F^s\} \tag{6}$$

2.2.2 Dual Rotor System

To achieve the equation of motion for the entire dual rotor system (figure 3) one must couple the equations of the two subsystems into the following form:

$$\begin{bmatrix} M^{r1} & 0 \\ 0 & M^{r2} \end{bmatrix} \begin{bmatrix} \ddot{u}^{r1} \\ \ddot{u}^{r2} \end{bmatrix} + \begin{bmatrix} G^{r1} & 0 \\ 0 & G^{r2} \end{bmatrix} \begin{bmatrix} \dot{u}^{r1} \\ \dot{u}^{r2} \end{bmatrix} + \begin{bmatrix} K^{r1} - K_c^{r1} & 0 \\ 0 & K^{r2} - K_c^{r2} \end{bmatrix} \begin{bmatrix} \dot{u}^{r1} \\ \dot{u}^{r2} \end{bmatrix} = \begin{bmatrix} F^{r1} \\ F^{r2} \end{bmatrix} + F_{ib} + F_b \tag{7}$$

Corresponding to eq. 7 the coupling of the two systems occurs by the inter bearing force $\mathrm{F_{ib}} + \mathrm{F_b}$ (eq. 5) at the joint location **C** of both rotors (figure 3).

3 Solutions of the System Equations

The key aspect of this work is to provide a fully modal description of the UHBR for the mentioned ROM, (Krukow and Dinkler, 2014). Thus the eigenvalues of the rotational system have to be determined at certain operation points.

3.1 Critical Speed

The critical speed corresponds to the natural frequency of the structure. Hence it then occurs when the excitation frequency equals the natural frequency. To determine the critical speed the homogeneous form of the eq. 6, respectively eq. 7 needs to be solved. The dynamic equation of the simplest form of an undamped rotor can be written as:

$$[M^s]\{\ddot{u}^s\} + [G^s]\{\dot{u}^s\} + [K^s]\{u\} = 0 \tag{8}$$

The solution of eq. 8 is an eigenvalue problem expressed by the form:

$$U = \Phi e^{j\lambda t} \quad \text{with} \quad \lambda = \alpha\omega \tag{9}$$

Inserted into eq. 8 this leads to the new eigenproblem

$$([K^s] - \lambda^2[\overline{M}^s])\Phi = 0 \text{ with } [\overline{M}^s] = [M^s] - j\frac{1}{\alpha}[G^s] \tag{10}$$

Depending on the respective reference system one has to transform the obtained results by Appendix B.

4 Validation Dual Rotor

4.1 Rotordynamic Modeling

For the purpose of validation, an analytical model of two co-axial counter rotating rotors from Ferraris et al. (1996) is used (figure 3). One disk mounted on the inner shaft rotating with the angular velocity Ω_{inner}. The outer rotor is made up of one disk mounted on the outer shaft rotating with the angular velocity $\Omega_{outer} = \Omega_{inner} \cdot n$. Whereas n represents the ratio of both spool angular velocities. Both rotors are axially symmetric with constant cross-sections. Non-symmetric effects are generated by the stiffness k_{xx}. They are supported by roller bearings at the points **A**, **B**, **C** and **D** in which the stiffness is considered to be numerically stiff. At the point **C** both rotor displacements are assumed to be congruent. The geometrical and physical parameters can be extracted from figure 3 and table 1, respectively.

Table 1
Geometrical and physical parameters

L = 0.4 m	R_1 = 0.02 m
H_1 = 0.03 m	R_2 = 0.15 m
H_2 = 0.03 m	R_3 = 0.03 m
E = $2 \cdot 10^{11}$ N/m^2	R_4 = 0.035 m
ρ = 7800 kg/m^3	R_5 = 0.1 m
$\mathrm{k_{bearings}} = 1 \cdot 10^{10}$ N/m	$k_{xx} = 8 \cdot 10^6$ N/m

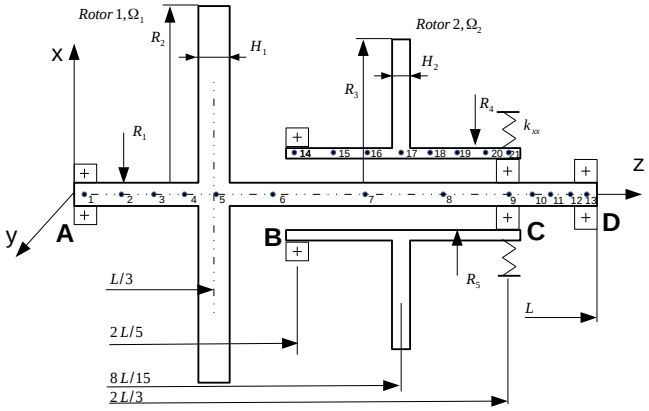

Fig. 3. Coaxial rotor model

4.1.1 Model Reduction

The methodology performed for building up each of the models is shown in figure 4. The right path shows the used standard approach for the FE model. The multi-body modeling, on the left side, starts in Ansys with the extraction of the required number of dynamical modes. Additionally a set of master nodes is chosen. The master nodes are needed as points of application in Simpack, to couple with other structures and induce external forces (e.g. bearing forces). The number of master nodes represents equal the number of static degrees of freedom of the flexible body with regard to their imprinted boundary conditions in Ansys. The following simulations include the linear acceleration, angular acceleration and constant rotation of the reduced structure and serve to generate the geometric stiffening matrix, which then is converted to the required flexible body input data.

4.1.2 Finite Element Modeling Approach

Initially the finite element models of the rotors were developed using the Ansys Parametric Design Language (APDL). Due to the necessity of capturing gyroscopic forces, geometric stiffening effects and simultaneously minimizing the numerical effort, the elements were chosen according to the proposal of (Qin and Chu, 2015) for rotating structures. 3D BEAM188 elements were chosen for the rotor shafts with a node distribution depicted in figure 3. The disks were assumed to be rigid, thus they were modeled with MASS21 elements. For the later application part the disks were modeled with SOLID185 and SOLID187 elements.

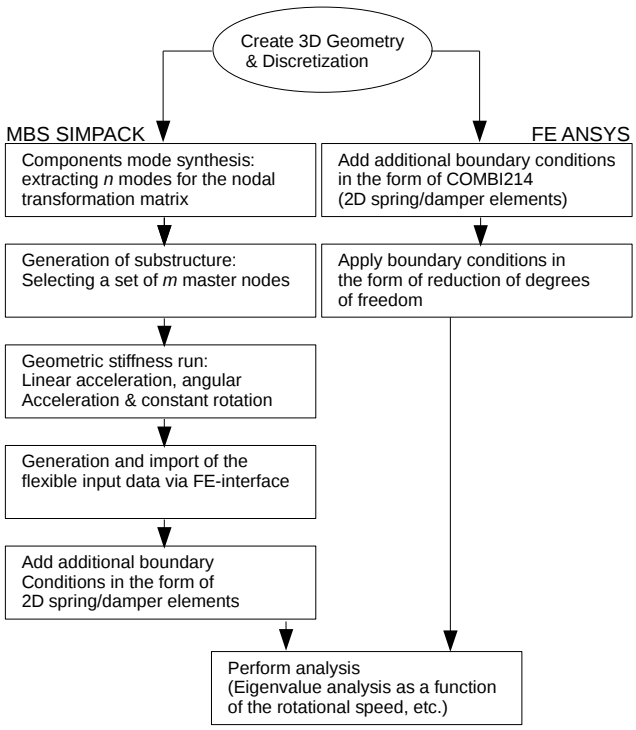

Fig. 4. Flow chart of the implemented methodology (Wallrap, 2007)

Table 2
Eigenvalues at standstill (Rotational speed $\Omega = 0$ rpm)

Analytical	**Simpack**	**Δ-Simpack**	**Ansys**	**Δ-Ansys**
166.59 Hz	168.80 Hz	1.30 %	168.24 Hz	0.99 %
190.93 Hz	190.55 Hz	0.20 %	189.82 Hz	0.58 %

The physical connection between those elements and the corresponding node of the shaft were modeled via contact element pairings (TARGE170/CONTA174). Each node was given 4 degrees of freedom, 2 translatory in x,y and 2 rotatory in Ω_x, Ω_y. The bearings were modeled as 2D spring-damper elements in lateral directions with the given parameters from table 1 in Simpack and Ansys, respectively. At point **A**,**B** and **D** the stiffness was chosen numerically stiff. Whereas for **C** only the stiffness in y-direction was numerically stiff, however not in x-direction causing an anisotropic behavior.

4.2 Validation and Simulation Results

In the following validation, the results shall legitimate the usage of Simpack for the respective purposes as part of the modal description in general and with high rotational velocities.

4.2.1 Eigenvalues

For the first part of the validation an eigenvalue analysis was performed for the non-rotating system ($\Omega = 0$) to assure, that the reduced model matches to finite element model properties and to the analytical values. Table 2 shows the comparison by absolute values and the relative error.

All errors are in an acceptable range around 1%. In regard to the requirements of the minimization of the numerical effort, the flexible shaft in Simpack was reduced down to the first 22 modes. The lack of higher frequencies causes this slight difference. Additionally all non-bending modes were excluded to meet the assumptions from Ferraris et al. (1996). Further reduction increases significantly the error. Only a massive increase of the range of modes lead to an improvement in accuracy, simultaneously quadratically increasing the numerical effort, though.

4.2.2 Campbell Diagram

The dependency of the eigenfrequency of the structure to the rotational velocity can be shown in a Campbell diagram. Therefore as the dynamic test case the rotational velocity was varied from Ω =0 to 20000 rpm in equidistant 1000 rpm steps. -1 was chosen for the rotating factor n. The minus sign indicates an opposing direction of rotation. For each step a critical speed analysis was performed for both Simpack and Ansys. Figure 5 shows the eigenfrequencies plotted over the rotor frequency. The results from the finite element computation are almost identical to the analytical and show an overall maximal error of 1%. The multibody simulation shows a good match with an overall maximum error of 3% at the maximum rotational frequency. There is a tendency of the error to grow towards higher rotational frequencies. This can be attributed to the 2% structural damping assigned to each mode that is needed in the Simpack model to attain numerical stability.

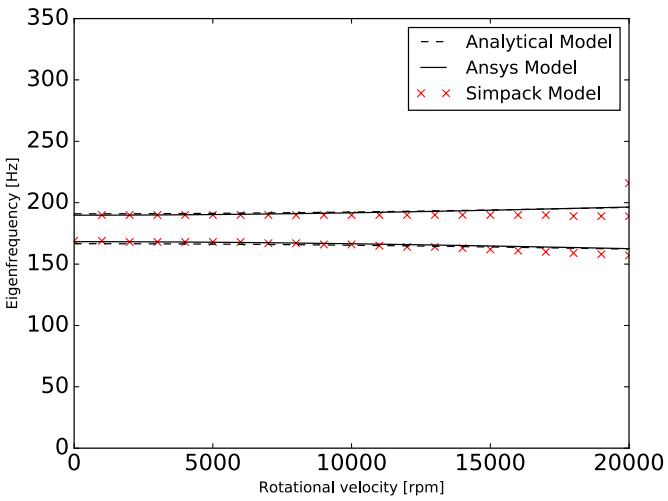

Fig. 5. Campbell diagrams of the three approaches

4.2.3 Unbalance Response

In the second part of the validation an unbalance response due to an eccentricity was performed. With respect to the rotational axis, a small mass is placed on the disk of the inner rotor causing an excitation of the system. The centrifugal force was modeled as a force element F acting on the center point of the disk and proportional to $\mathrm{m_u d} \cdot \Omega^2$. The product $\mathrm{m_u d} = 10^{-7}\,\mathrm{kgm}$ characterizes the mass unbalance situated away from the center point. Figure 6 shows the results of the analytical model and the results from Simpack performed with the integrated "Linear System Analysis" module. The range of the excitation frequency was chosen within the range of 0 to 20000 rpm, corresponding to a 1/rev excitation. As expected, with regard to the Campbell diagram in figure 5, two frequencies are taken into account. On the one hand the frequency branch starting at 166.59 Hz, represents the backward whirl.

Table 3
Comparison of the rotational frequencies of the unbalance response

Analytical	Simpack	Δ-Simpack	Ansys	Δ-Ansys
165.32 Hz	168.41 Hz	1.87 %	163.33 Hz	1.20 %
192.83 Hz	190.35 Hz	1.28 %	188.33 Hz	2.27 %

And on the other hand the top branch starting at 190.93 Hz, represents the forward whirl. The qualitative behavior of both results is in good agreement compared to the analytical ones. Table 3 shows the comparison of the resonance peaks with an acceptable error around 2%. One has to mention the third excitation peak for the Ansys results at 328.33 Hz representing the excitation of the second bending mode which could not be excluded but neither has to be taken into account. The analytical model takes only considers the first mode, so does the Simpack model.

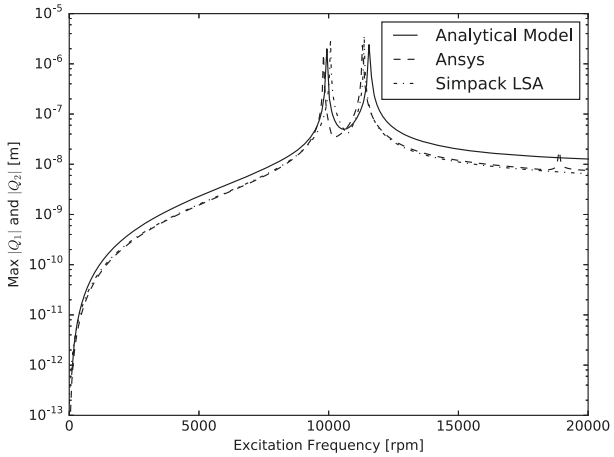

Fig. 6. Comparison of the unbalance responses

5 Application to an UHBR Engine

5.1 Rotordynamic Model

The investigated configuration of the ultra-high bypass ratio engine is shown in figure 7 a). The bypass ratio, i.e. the ratio of the outer mass flow referred to the inner, core mass flow is 17. The ensuing geometric consequence is a characteristically large diameter of the fan equal 2.1 m. The remaining essential global system parameters are shown in table 4.

The principal layout of the investigated UHBR configuration is depicted in figure 7 b). The model is divided into three groups including the Fan and its shaft. The inner low pressure unit consists of the booster with three stages and the turbine with four stages. Whereas the outer high pressure unit operates with eight compressor stages and two turbines stages. The bearings for each driving unit are located at the points **A**-**F**. **A**/**B** belong to the Fan, **C**/**D** belong to the low pressure and **E**/**F** to the high pressure unit. The connection from the low pressure shaft (at node 16) and the fan (at node 8) is realized with a force element which simulates a planetary gear. The gear ratio equals $i = \frac{n_{Fan}}{n_{LP\ Shaft}} = 0.315$ whereby the ratio of the rotational speed of the inner and outer shaft equals $n = \frac{n_{HP\ Shaft}}{n_{LP\ Shaft}} = -1.32$. The minus sign indicates an opposing

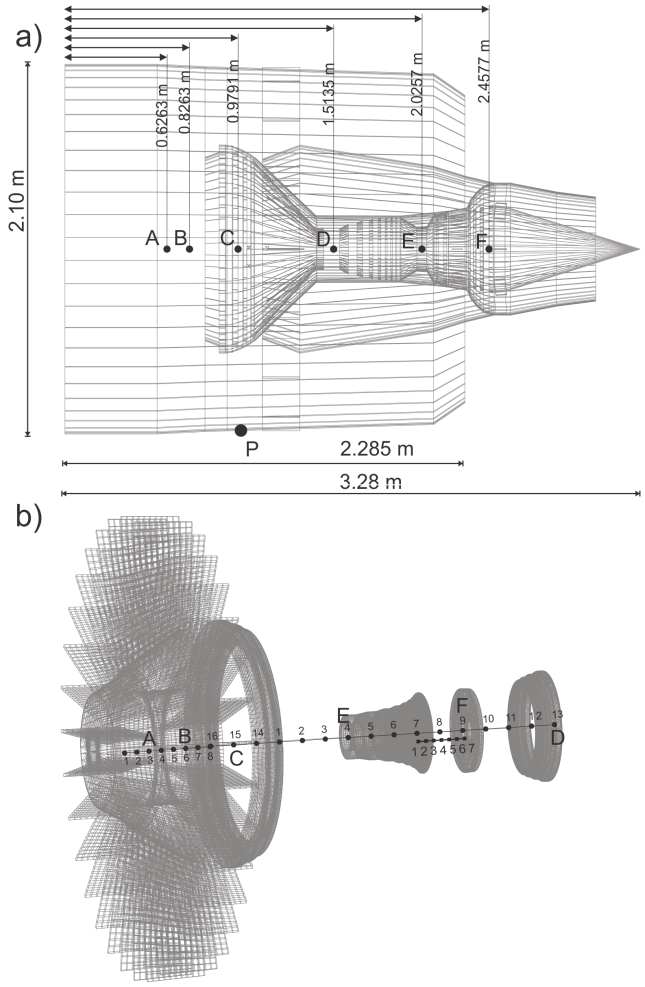

Fig. 7. a) Cross-section of the UHBR engine housing b) Nodal distribution of the driving units

Table 4
Resulting physical system parameters

Component	Mass	CoG [x]	Inertia I_1	Inertia $I_{2,3}$
Total	2021.42 kg	1.174 m	1017.71 kgm^2	1424.2 kgm^2
FAN & Shaft	611.35 kg	0.653 m	149.38 kgm^2	78.21 kgm^2
LP Unit	175.62 kg	1.488 m	32.62 kgm^2	91.18 kgm^2
HP Unit	85.30 kg	1.85 m	1.52 kgm^2	3.65 kgm^2

direction of rotation. As design point for the investigations the operating point of the aircraft at its highest altitude, the so called "Top Of climb", was chosen. Consequently the operating parameters are the following $\Omega_{LP} = 13690$ rpm, $\Omega_{HP} = 18049$ rpm and $\Omega_{FAN} = 4346$ rpm.

For the tradeoff of numerical effort and accuracy, the scope of the modal description was set as follows:

Component	f_{max}	Number of modes
LP Unit	3000 Hz	10
HP Unit	7000 Hz	11
Fan	12000 Hz	7

The representing modes are only bending modes. No expanding or torsional modes are considered. These are symmetric (to the rotational axis) modes which do not cause a change in the direction of the angular momentum and hence not inducing any forces on the shaft.

5.2 Bearing Dynamics

The non-linear dynamics of the bearings were realized by the qualitative implementation of the model of Lee (1993). Figure 8 shows the normalized stiffness(damping) to the stiffness(damping) at 0 rpm in lateral direction. The model parameters for every bearing were determined by the use of the procedure presented in subsection 5.4. For the sake of simplicity of the model neither sealing effects nor lateral/axial clearance were taken into account. The mathematical description can be found in A.

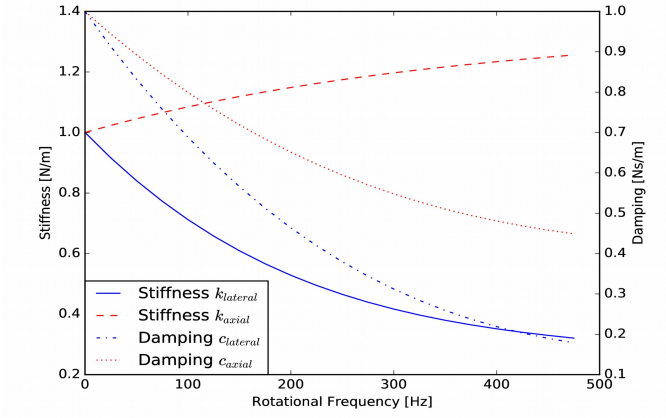

Fig. 8. Normalized dynamical stiffness and damping coefficients as a function of the rotational velocity, (Lee, 1993)

5.3 Critical Speed Map

A crucial parameter in the design process is the stiffness of the support system of the shafts. The reason is to prevent an intersection of the frequency of the operating point with the eigenfrequency of the system to prevent resonance or to place the intersection in a uncritical range. By varying the bearing stiffness of the undamped system the significant influence of the stiffness parameters can be shown. Therefore the critical speed map was generated for all three support systems. In figure 9 there are the first three critical speeds as a function of the lateral stiffness plotted. Since the support system of all three units has the same generic setup, they all show qualitatively a similar behavior, therefore the low pressure unit serves exemplarily. The first two critical speeds show a strong dependency on the bearing stiffness up to 10^9 N/m for the first and up to 10^8 N/m for the second one, respectively. The third critical speed is nearly independent from the stiffness parameters becoming numerically stiff above 10^{10} N/m. Whereas the first critical speed of the low pressure unit decreases in its dependency above 10^6 N/m. The second critical speed behaves similar to the one of the same-named from the other components. The behavior of the third critical speed is straightened out and shows a strong dependence within the range of 10^6 to 10^{10} N/m and from 10^7 to 10^9 N/m. Therefore the stiffening parameters had to be chosen carefully by taking into account the non-linear behavior to prevent the intersection of the system frequency and operating frequency.

5.4 Determination of the Stiffening Parameters

The initial values of the stiffening parameters ($\Omega = 0$) were determined by evaluating a design of experiment (DoE)

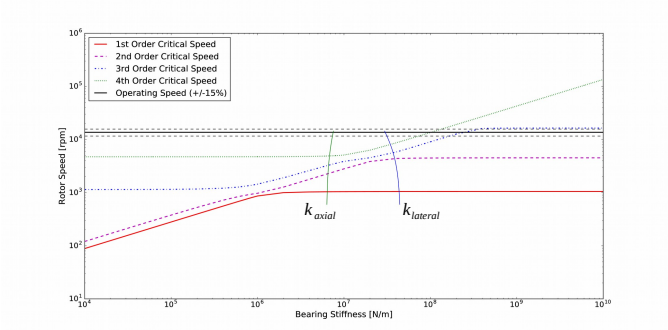

Fig. 9. Critical speed maps with speed-dependent stiffness parameters (k_{yy} and k_{zz})of the low pressure unit

Table 5
Bearing parameters

Component	Initial Stiffness [N/m]	Stiffness at Design Point [N/m]	Initial Damping [Ns/m]
LP Unit	$4.53 \cdot 10^7$	$3.0 \cdot 10^7$	1000
HP Unit	$5.54 \cdot 10^7$	$3.5 \cdot 10^8$	1000
FAN Unit	$8.54 \cdot 10^7$	$7.0 \cdot 10^8$	3000

varying an excitation force and the radial stiffness parameter. The excitation force was modeled as unbalance force ($F_{unbalance} = m_u d \cdot \Omega^2$, with $m_u d = 10^{-6}$ kgm). The results of the low pressure driving unit are shown in figure 10 exemplarily for the methodology. The excitation frequency varies from 0 Hz to 250 Hz with 500 subsets located at the low pressure compressor stage 3, while varying the lateral stiffness from 10^7 N/m to 10^{10} N/m. Minimizing the amplitude at the given point the determination of the stiffening parameters needs to be placed within an adequate separation margin of 15-20% away from the operating speed (figure 9) (Yoon et al., 2013).

Exciting the low pressure turbine leads to this trade-off of the listed parameters at the design point and consequently to their initial values (table 5).

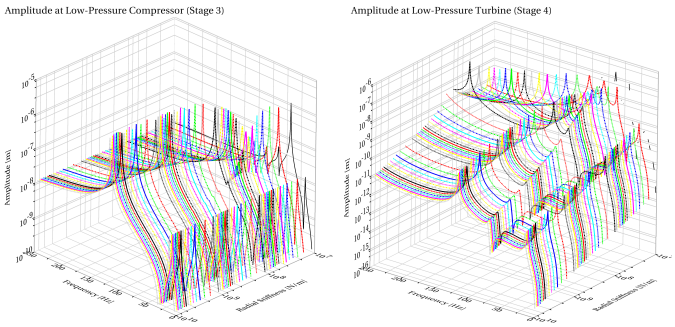

Fig. 10. Results of the DoE of the low pressure units. Measured amplitude in lateral direction.

5.5 Campbell Diagram

Due to the large rotating masses of the compressor and turbine stages the gyroscopic forces are considered. It is essential to evaluate the dependence of the eigenfrequency to the rotational velocity. The results are shown in figure 11 for all the components with respect to their corresponding rotational velocities.

To have a better understanding of the mode coupling the results are calculated in the rotational system.

Table 6
Frequencies of the different modes depending on the roational speed

Mode No.	Un-/damped frequency at $\Omega = 0$ rpm f [Hz]	Undamped frequency at $\Omega = 9000$ rpm f [Hz]	Damped frequency at $\Omega = 9000$ rpm f_0 [Hz]
1	17.4952	63.1204	71.0640
2	17.4952	63.4306	70.4299
3	70.8584	69.4532	70.9838
4	70.8584	70.7624	70.7640
5	82.3787	71.9361	73.6017
6	82.3787	78.3674	78.3833
7	153.201		
8	153.201		

Considering the results in the inertial system one has to transform the frequencies via Appendix B. For the low pressure units the first five modes, for either the high pressure unit and the fan the first two modes are plotted in the Campbell diagram.

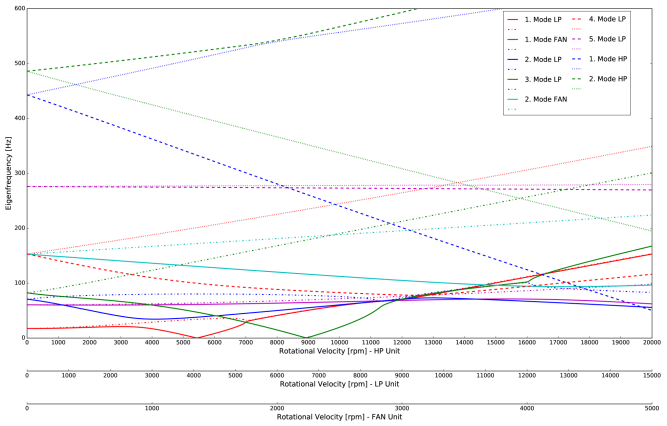

Fig. 11. Campbell Diagram of the complete System

Due to the fact that multiple disks on the low pressure unit are mounted asymmetrically (figure 12) a tilting in every modeshape is present. Thus each modeshape has a change in the direction of the rotational axis and thus a change in the angular momentum. Hence every eigenfrequency depends on the rotational speed Ω. Around 9000 rpm the first four bending modes tend to a strong coupling, all of them resulting in an identical modeshape (figure 13). The frequencies of this conglomerate of modes are located around 70-80 Hz (compare table 7).

The coupling of these single branches of the second and third mode does not split until 12000 rpm. Considering the displacements of the different modeshapes (compare figure 12) a region of maximum displacement can be identified and attributed to node 9. Therefore this node was chosen as the application point for the unbalance excitation.

For the first fan mode a tilting of the fan occurs causing a softening/stiffening effect, hence there is no splitting in the rotational system of the eigenfrequencies. Whereas for the second bending mode no tilting occurs and the split is based on the rotational speed. The behavior of the high pressure shaft can be compared to a beam without disk. For the first two bending modes no stiffening can be detected. Around 9000 rpm there is a slight coupling of the increasing branches that occurs.

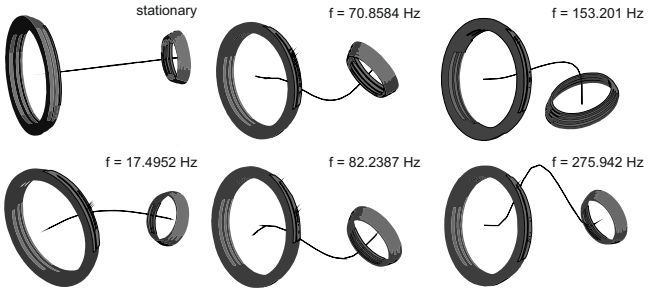

Fig. 12. Modeshapes of the low pressure unit at $\Omega = 0$rpm

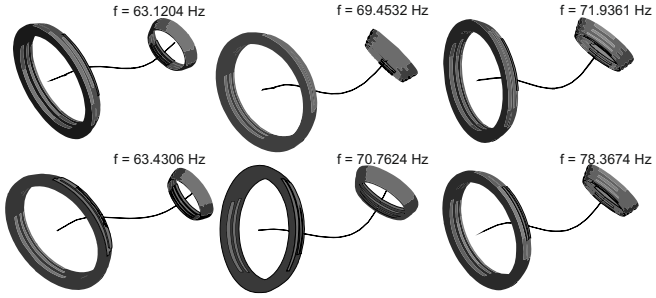

Fig. 13. Modeshapes of the low pressure unit at $\Omega = 9000$rpm

5.6 Unbalance Response

To evaluate the behavior of the system to a synchronous excitation (matching the rotational speed of the shaft) an unbalance force induced in the system. Figure 14 shows the unbalance response as lateral amplitude in x direction, dependent on the point of application and excitation frequency. Nodes 1 to 12 can be attributed to the middle part of the rotor, node 13 is located at the bearing point of the low pressure turbine and node 14, 15 and 16 are located at the low pressure compressor. Since the bearings are symmetric and isotropic and, compared to the validation model, there is no counter rotating shaft exciting the opposing whirl, only the forward whirling modes are excited due to the unbalance force (Gasch et al., 2005). Four peaks of the amplitude can be detected (figure 15). The excited frequencies corresponding to the peaks are at 18 Hz, 71 Hz, 82 Hz and 153 Hz.

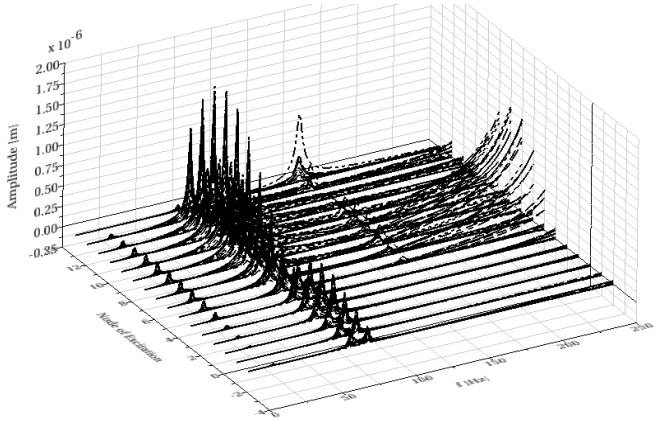

Fig. 14. Variation of the location of the unbalance force

The maximum amplitudes are detected for the second and third mode for each simulation at the 9th node. These results are consistent with the calculated modeshapes (figure 12). Hence for the system, both the second and third mode at 71 Hz and 82 Hz are the critical ones regarding unbalance forces.

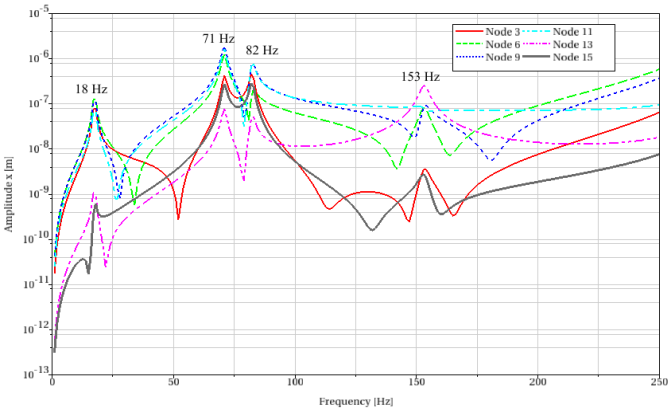

Fig. 15. Unbalance response forced by excitation at node 9

5.7 Waterfall Diagram

Exciting the system at the bearing points as a form of ground vibration leads to the overall vibration response of the system, respectively the sensitivity to vibration. The vibration itself was modeled as a sinusodial excitation in 250 steps from 0 Hz to 250 Hz while increasing linear the rotational velocity from 0 Hz to 250 Hz in 51 simulations. The results are shown in figure 16. Three significant peaks can be detected. The first one occurs at a rotational velocity of Ω =5250 rpm at 29 Hz located on the coupling point of first and second bending mode. The second peak can be ascribed to the forward whirling mode of the third mode reaching its maximum at $\Omega = 7950$ rpm upon 33 Hz. The third peak at 12150 rpm emerges out of the decoupling of one of second and third eigenfrequency branches at 109 Hz.

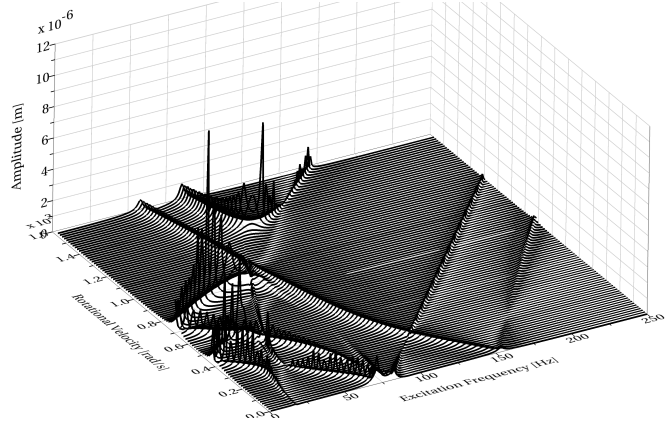

Fig. 16. Waterfall diagram of the LP unit, amplitude measured at node 9

5.8 Transient Behavior - Required Complexity

One has to keep in mind that these investigations merely serve as the preparation for the later investigation of the interaction between the UHBR engine and the wing structure. Hence the transient startup serves not only as an additional identification of the overall system behavior but a consideration of the required complexity of the model. Therefore the time dependent behavior was examined via simulating the start-up of the engine without considering gravitational forces. Based on the system response, an evaluation should be made about the necessary complexity of the model. The rotational velocity was increased linearly over $T_{Start} = 20$ s from $\Omega_{LP} = 0$ to 13690 rpm and $\Omega_{HP} = 0$ to 18049 rpm, respectively, followed by $T_{konst} = 10$ s with constant rotational velocity (figure 17 a)). The complexity of the model was varied by taking all modes, no modes and the modes exclusively from each unit into account. Considering only the transmitted forces at the interface point (P figure 7 b)) leads to an discrepancy of 12.5% in the amplitude if none or only the LP, HP modes are included. To take the transmitted frequency range into account an unbalance force was placed at Node 9 (LP Unit: $mu_d = 10^{-6}$kgm), Node 5 (HP Unit: $mu_d = 10^{-6}$kgm) and Node 4 (Fan Unit: $mu_d = 10^{-4}$kgm). Thus the response at the interface point is a sum of each one of the 1/rev excitations of each respective rotational unit.

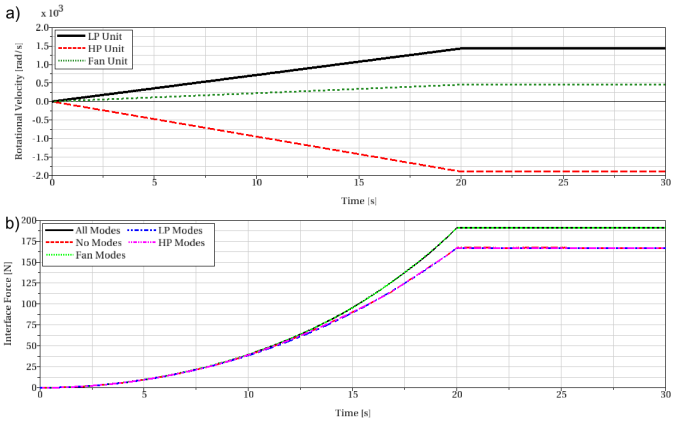

Fig. 17. a) Rotational Velocity during Startup b) Interface force of the transient startup without an external excitation

Fig. 18 shows the frequency spectrum of the response normalized to the respective excitation force.

Considering all modes there are 6 peaks detected, at 66 Hz, 117 Hz, 154 Hz, 311 Hz, 373 Hz and 529 Hz. The peaks at 154 Hz and 373 Hz are excitations due to implemented the start-up curve. After the 20 second interval of linear acceleration, the acceleration instantaneously becomes zero, exciting both the low and high pressure unit.

The best agreement, by means of modal similarity, shows the case with exclusively modes from the HP unit. A moderate agreement can be found between 80 Hz and 140 Hz if exclusively LP modes are considered, showing an excellent agreement above 140 Hz, though. Although the case in which only Fan modes are considered, the transmitted forces correspond to the reference case, this does not apply the spectral range. As expected if no modes are included the agreement is poor. The combination of Fan and LP modes slightly increases the accuracy since both are connected via the gear, which is numerically implemented as a constraint and therefore couples both of the systems. However this case would not decrease the complexity significantly.

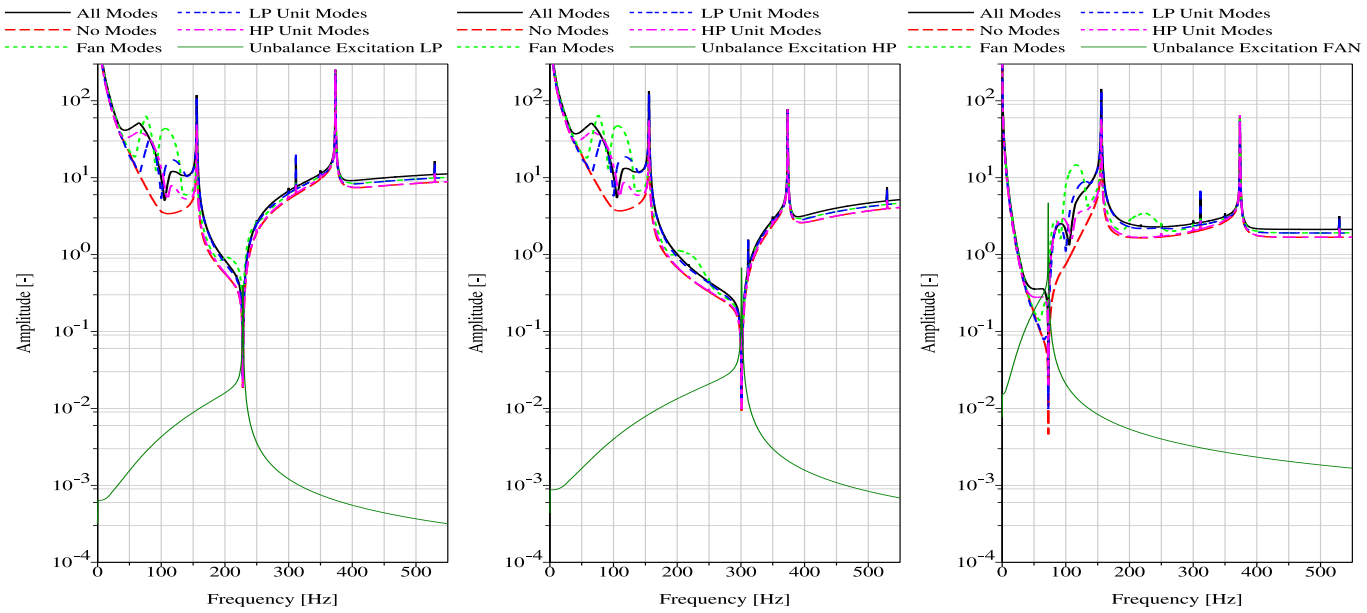

Fig. 18. Response of the interface point referred to each respective excitation forces

6 Conclusion

A rotor dynamic analysis was performed for a twin rotor model with coaxial counter rotating shafts in order to validate this analytical system with the multi body simulation program Simpack and the finite element tool Ansys. Both the eigenvalue analysis depending on the rotational speed and the system response due to an unbalance excitation show a good agreement with the expected values. However Simpack shows a slight error due to the need of damping. Simultaneously the validation legitimizes the presented methodology for the modal reduction technique.

The methodology was applied to an UHBR engine and a rotor dynamic analysis was performed. The stiffness parameters were determined via a critical speed diagram. Due to gyroscopic forces the eigenfrequencies of the low pressure unit changed leading to a wide speed range in which the eigenmodes tend to couple and become similar in their shape. Thereby the critical modes were identified and used for an unbalance excitation confirming the assumption. The examination of different model complexities by their output a certain interface point showed the need of the complete rotational system to be modally described. However the effective influence on connected structures, e.g. a wing-pylon, especially under the influence of gravitational forces have not been taking into account yet and will be addressed in future work.

Acknowledgment

The authors would like to thank Dr. Oliver Hach from the Institute of Aeroelasticity for his support. Financial support has been provided by the German Research Foundation (Deutsche Forschungsgemeinschaft, DFG) in the framework of the Sonderforschungsbereich 880.

Appendix

Appendix A
Non-linear bearing dynamics model

Stiffness parameter :

$$k_{xx}(\Omega) = 1 - 3.52e^{-3}\Omega + 7.06e^{-6}\Omega^2 - 6.77e^{-9}\Omega^3 + 2.46e^{-12}\Omega^4 \tag{11}$$

$$k_{yy}(\Omega) = \frac{1}{4}(1 + 9.67e^{-4}\Omega - 1.31e^{-6}\Omega^2 + 1.02e^{-9}\Omega^3 - 3.35e^{-13}\Omega^4) \tag{12}$$

Damping parameter:

$$d_{xx}(\Omega) = 1 - 3.6e^{-3}\Omega + 5.07e^{-6}\Omega^2 - 2.38e^{-9}\Omega^3 \tag{13}$$

$$d_{yy}(\Omega) = \frac{1}{4}(1 - 2.3e^{-3}\Omega + 3.06e^{-6}\Omega^2 - 1.39e^{-9}\Omega^3) \tag{14}$$

Appendix B
Transformation from rotating to inertia fixed coordinates

Backward whirl modes, characterized by increasing frequencies:

$$f_{Inertial} = |f_{Rotating} - \frac{\Omega}{2\Pi}| \tag{15}$$

Forward whirl modes, characterized by decreasing frequencies before mirroring at the zero frequency line:

$$f_{Inertial} = f_{Rotating} + \frac{\Omega}{2\Pi} \tag{16}$$

Forward whirl modes, characterized by decreasing frequencies after mirroring at the zero frequency line:

$$f_{Inertial} = -f_{Rotating} + \frac{\Omega}{2\Pi} \tag{17}$$

Appendix C
Geometrical Paremters UHBR

The parametrized geometrical values were determined via:

$$value_{current} = value_{origin} \cdot (Factor)^{\text{Stage Number}-1}$$

Table 7
Geometrical ratios for parametrization

LP Compressor			
Geometrical		Factor	
r_{inner}	$= 0.46$ m	i_{inner}	$= 0.99$
r_{outer}	$= 0.56$ m	i_{outer}	$= 0.96$
$width_{Disk}$	$= 0.035$ m	i_{Disk}	$= 0.7$
$width_{Disk}$	$= 0.029$ m	i_{Disk}	$= 0.71$
LP Turbine			
Geometrical		Factor	
r_{inner}	$= 0.21$ m	i_{inner}	$= 1.05$
r_{outer}	$= 0.216$ m	i_{outer}	$= 1.05$
$width_{Drum}$	$= 0.011$ m	i_{Drum}	$= 1.3$
$width_{Drum}$	$= 0.011$ m	i_{Drum}	$= 1.3$
HP Compressor			
Geometrical		Factor	
r_{inner}	$= 0.062$ m	i_{inner}	$= 0.922$
r_{outer}	$= 0.1$ m	i_{outer}	$= 1.09$
$width_{Disk}$	$= 0.059$ m	i_{Disk}	$= 0.72$
$width_{Disk}$	$= 0.05$ m	i_{Disk}	$= 0.72$
HP Turbine			
Geometrical		Factor	
r_{inner}	$= 0.052$ m	i_{inner}	$= 1.08$
r_{outer}	$= 0.19$ m	i_{outer}	$= 0.99$
$width_{Drum}$	$= 0.0122$ m	i_{Drum}	$= 1.4$
$width_{Drum}$	$= 0.012$ m	i_{Drum}	$= 1.42$

REFERENCES

H-W D. Chiang and C-N. Hsu. Rotor-bearing analysis for turbomachinery single- and dual-rotor systems. *Journal of Propulsion and Power*, 2004.

R. R. Jr. Craig and M. C. C. Bampton. Coupling of substructures for dynamic analysis. *AIAA Journal*, 6(7):1313–1319, 1986.

Z-X. Fei, S-G. Tong, and C. WeiWei. Investigation of the dynamic characteristics of a dual rotor system and its start-up simulation based on finite element method. *Journal of Zhejiang University-Science*, 2013.

G. Ferraris, V. Maisonneuve, and M. Lalanne. Prediction of the dynamic behavior of non-symmetric coaxial co- or counter-rotating rotors. *JSV*, 1996.

Robert Gasch, Rainer Nordmann, and Herbert Pfuetzner. *Rotordynamik*. Springer, 2005.

Ian Krukow and Dieter Dinkler. A reduced-order model for the investigation of the aeroelasticity of circulation-controlled wings. *CEAS Aeronaut Journal*, 5(2):145–156, 2014.

Chong-Won Lee. *Vibration Analysis of Rotors*. 21. Springer Netherlands, 1993.

Z.Y. Qin and F.L. Chu. Finite element modmodel techniques for rotors with cylindrical shells. *IFToMM World Congress*, 2015.

Rolf Radespiel and Wolfgang Heinze. Sfb 880: Fundamentals of high lift for future commercial aircraft. *CEAS Aeronaut Journal*, 5(239-251), 2013.

Stefan Waitz and Holger Hennings. The aeroelastic impact of engine thrust and gyroscopics on aircraft flutter instabilities. *IFASD*, 2015.

Oskar Wallrap. Standardization of flexible body modeling in multibody system codes, part i: Definition of standard input data. *Mechanics of Structures and Machines*, 2007.

Se Young Yoon, Zongli Lin, and Paul E. Allaire. *Control of Surge in Centrifugal Compressors by Active Magnetic Bearings*. Springer, 2013.